A framework for characterizing structural uncertainty in large-eddy simulation closures

Lluís Jofre[a], Stefan P. Domino[b], Gianluca Iaccarino[a]

[a]*Center for Turbulence Research, Stanford University, Stanford, CA 94305, USA*
[b]*Computational Thermal and Fluid Mechanics, Sandia National Laboratories, Albuquerque, NM 87185, USA*

Abstract

Motivated by the sizable increase of available computing resources, large-eddy simulation of complex turbulent flow is becoming increasingly popular. This technique reduces by several orders of magnitude the computational cost of simulating turbulence in comparison to directly resolving all the flow scales. The reduction in cost is a direct consequence of a filtering operation that enables to represent only large-scale motions. However, the small-scale fluctuations and their effects on the resolved flow field require additional modeling. The assumptions made in the closure formulations become potential sources of incertitude that can impact the quantities of interest. The objective of this work is to introduce a framework for the systematic estimation of structural uncertainty in large-eddy simulation closures. In particular, the methodology proposed is independent of the initial model form, computationally efficient, and suitable to general flow solvers. The approach is based on introducing controlled perturbations to the turbulent stress tensor in terms of magnitude, shape and orientation, such that propagation of their effects can be assessed. The framework is rigorously described, and physically plausible bounds for the perturbations are proposed. In order to test its performance, a comprehensive set of numerical experiments are reported for which physical interpretation of the deviations in the quantities of interest are discussed.

Keywords: large-eddy simulation, predictive science, turbulence modeling, uncertainty quantification

1. Introduction

Over the past decade, large-eddy simulation (LES) has gained significant popularity as a high-fidelity (HF) reference technique for the numerical resolution of complex turbulent flow. For example, it has been successfully applied to the study of reactive flow in industrial gas turbine combustors [1, 2, 3], for which experimental data is difficult and expensive to acquire due to the elevated pressures and temperatures typically achieved under operational conditions. One of the main reasons for this increase in popularity is the tremendous growth in available computational power, which has made its superior accuracy attractive with respect to other strategies like the Reynolds-averaged Navier-Stokes (RANS) equations. Moreover, despite the presumably further increase in computing resources through the deployment of upcoming exascale supercomputers — 1-10k times augmented floating-point capacity is foreseen [4] —, the expectation in the computational community is that LES will continue its consolidation as a workhorse methodology for engineering applications and multiscale problems, whereas direct numerical simulation (DNS) will remain as the gold standard technique, affordable only in very controlled scientific studies. In comparison to DNS, LES approaches reduce the computational cost of solving turbulent flow by removing small-scale information from the governing equations via low-pass filtering. However, the effects of the small scales on the resolved flow field are often not negligible, and therefore their contribution in the form of subfilter stresses needs to be modeled. As a result, the assumptions introduced in the closure formulations become potential sources of structural uncertainty that can affect the quantities of interest (QoI).

Email addresses: jofre@stanford.edu (Lluís Jofre), spdomin@sandia.gov (Stefan P. Domino), jops@stanford.edu (Gianluca Iaccarino)

A significant number of studies have been dedicated to identify sources of error resulting from the numerical approximations required to discretely solve the LES governing equations. Some of the most notable works are the seminal paper by Ghosal [5] and the detailed error database gathered by Meyers et al. [6]. However, even with the widespread utilization of LES in many scientific and technological areas, there have been few studies in which model-form incertitude has been analyzed from an uncertainty quantification (UQ) viewpoint. In general, most analyses are based on non-intrusive methodologies applied to simple flow configurations, and are concerned mainly with sensitivities to LES closure parameters, such as model coefficients [7], filter characteristics [8] or mesh resolution [9]. A more sophisticated approach is to consider the closure parameters uncertain, and estimate their effects on the QoIs by forward-propagating them as probability distributions. This strategy has been applied to RANS [10] and LES [11] models, and extended to incorporate experimental data by means of data-assimilation [12] and machine learning techniques [13]. In the case of complex flows, some methodologies perform predictions based on an ensemble of solutions obtained using different models, as for example in earth sciences for weather and ocean forecasting [14, 15]. All these approaches, although useful from the practitioner's perspective, present important impediments to generalization due to their dependency on the underlying structure of the models utilized. In this regard, the present work aims at developing a framework for the methodical estimation of structural uncertainty in LES closures that is independent of the initial model form, computationally efficient and suitable to general LES solvers.

The framework proposed feeds from the methodology previously introduced in the context of RANS approaches [16, 17], although it contains important differences due to the inherent distinction between the two turbulence-resolution techniques. In short, the strategy is based on introducing perturbations to the decomposed turbulent stress tensor within a range of physically plausible values. These correspond to discrepancy in magnitude (trace), shape (eigenvalues) and orientation (eigenvectors) of the normalized subfilter stresses with respect to a given tensor state. In this paper, the UQ framework is presented in detail and a comprehensive set of numerical experiments are performed. First, the conservation equations governing LES, together with a description of the eddy-viscosity closure group, are summarized in Section 2. A detailed analysis of the filtered advection term and its representation in terms of the barycentric map is discussed in Section 3. In Section 4, the methodology is derived and physical bounds for structural incertitude estimation are proposed. A consistent set of numerical results for turbulent channel flow are reported in Section 5. Finally, conclusions are drawn and future work is outlined in Section 6.

2. Large-eddy simulation equations

The governing LES equations are derived by applying a low-pass filter, G, to the Navier-Stokes equations. The filter decomposes any flow variable $\phi(\mathbf{x}, t)$ into large-, $\overline{\phi}$, and small-scale, ϕ', contributions, i.e., $\phi = \overline{\phi} + \phi'$. The filtered part is defined as

$$\overline{\phi}(\mathbf{x}, t) = \int_{\Omega} G(\mathbf{x}, \mathbf{x}', \Delta)\phi(\mathbf{x}', t)\, d\mathbf{x}', \tag{1}$$

with $\mathbf{x}$ and $\mathbf{x}'$ position vectors in the domain Ω, and Δ the characteristic width of the filter.

Assuming that differentiation and filtering commute [18, 19], the filtered incompressible continuity and Navier-Stokes equations result in

$$\frac{\partial \overline{u}_i}{\partial x_i} = 0, \tag{2}$$

$$\frac{\partial \overline{u}_i}{\partial t} + \frac{\partial (\overline{u_i u_j})}{\partial x_j} = -\frac{1}{\rho}\frac{\partial \overline{p}}{\partial x_i} + \nu \frac{\partial^2 \overline{u}_i}{\partial x_j \partial x_j}, \tag{3}$$

where u_i and p are the velocity vector and pressure variables, and ρ and ν are the density and kinematic viscosity of the fluid. This system is undetermined since it contains more unknowns ($\overline{u}_i$, $\overline{u_i u_j}$, $\overline{p}$) than equations. Hence, in order to advance the solution of the filtered quantities in time, a closure definition for the nonlinear filtered advection term, $\overline{u_i u_j}$, needs to be provided, as well as boundary conditions and an initial state for $\overline{u}_i$ and $\overline{p}$.

In a LES framework, Leonard's decomposition [20] separates $\overline{u_i u_j}$ into a large-scale part, $\overline{u}_i \overline{u}_j$, and a subfilter scale (SFS), or turbulent, stress tensor, τ_{ij}, i.e., $\overline{u_i u_j} = \overline{u}_i \overline{u}_j + \tau_{ij}$. Therefore, the conservation of filtered momentum can be recast in the form

$$\frac{\partial \overline{u}_i}{\partial t} + \frac{\partial (\overline{u}_i \overline{u}_j)}{\partial x_j} = -\frac{1}{\rho}\frac{\partial \overline{p}}{\partial x_i} + \nu \frac{\partial^2 \overline{u}_i}{\partial x_j \partial x_j} - \frac{\partial \tau_{ij}}{\partial x_j}. \tag{4}$$

The resolved scales of LES, $\overline{\phi}$, are characterized by the filter applied to the conservation equations. In a general context, the filtering and discretization operators are different [21]. However, in most cases the spatial discretization is chosen to be specifically the low-pass filter [22], and therefore τ_{ij} is habitually referred to as the subgrid-scale (SGS) tensor.

2.1. Subgrid-scale models

The objective of SGS models is to replace the unknown value of τ_{ij} by an approximate representation. In order to clearly differentiate τ_{ij} from its approximation, τ_{ij}^{sgs} will be used in this paper to refer to the modeled τ_{ij}. Many different models for τ_{ij}^{sgs} exist [23, 24, 25, 26]. However, the eddy-viscosity assumption [22] is the most popular closure due to its robustness and ease of implementation. This group of models represents the anisotropic part of τ_{ij} as

$$\tau_{ij}^{sgs} - \frac{\tau_{kk}^{sgs}}{3}\delta_{ij} = -2\nu_{sgs}\overline{S}_{ij}, \tag{5}$$

where $\tau_{kk} = \tau_{11} + \tau_{22} + \tau_{33}$ is the trace of the tensor, δ_{ij} is the Kronecker delta, ν_{sgs} is the turbulent viscosity given by a specific model [27, 28, 29, 30, 31], and $\overline{S}_{ij} = 1/2(\partial\overline{u}_i/\partial x_j + \partial\overline{u}_j/\partial x_i)$ is the strain rate tensor of the resolved scales. As it can be observed in the above equation, the different eddy-viscosity models only differ in the evaluation of ν_{sgs}. Therefore, they only account for variability in the magnitude of the tensor, while the anisotropy and orientation are directly determined by $\overline{S}_{ij}$. In other words, this group of models focuses only in one of the six degrees of freedom in τ_{ij}. In addition, as it will be analyzed in Sec. 5.1, its particular construction is such that it is inherently dissipative, and therefore this group of models is typically combined with low-dissipation numerical schemes [32]. For example, the Wall-Adapting Local Eddy-Viscosity (WALE) model [29] evaluates the turbulent viscosity as

$$\nu_{sgs} = (C_w\Delta)^2 \frac{\left(\mathcal{S}_{ij}^d\mathcal{S}_{ij}^d\right)^{3/2}}{\left(\overline{S}_{ij}\overline{S}_{ij}\right)^{5/2} + \left(\overline{S}_{ij}\overline{S}_{ij}\right)^{5/4}} \quad \text{and} \quad \mathcal{S}_{ij}^d = \frac{1}{2}\left(\overline{g}_{ij}^2 + \overline{g}_{ji}^2\right) - \frac{\overline{g}_{kk}^2}{3}\delta_{ij}, \tag{6}$$

with C_w a model coefficient ($C_w = 0.325$ based on homogeneous isotropic turbulence data), Δ the subgrid characteristic length scale (in practice the size of the mesh), and $\overline{g}_{ij} = \partial\overline{u}_i/\partial x_j$ the velocity gradient tensor of the resolved scales.

An additional parameter requiring modeling is the trace of the tensor, τ_{kk}^{sgs}, as it has been subtracted from τ_{ij}^{sgs} in Eq. 5. However, in LES of incompressible flows, the isotropic part, $\tau_{kk}^{sgs}/3$, is usually added to the filtered pressure, resulting in a modified pressure that the LES solver evolves in time. In the case of compressible flows, explicit subgrid models have been proposed for τ_{kk}^{sgs}, like for example the parametrization by Yoshizawa [33]

$$\tau_{kk}^{sgs} = 2C_I\Delta^2\left|\overline{S}\right|^2 \quad \text{with} \quad \left|\overline{S}\right| = \left(2\overline{S}_{ij}\overline{S}_{ij}\right)^{1/2}, \tag{7}$$

where C_I is a model coefficient that can be approximated, for instance, as proposed by Moin et al. [34].

3. Nonlinear filtered advection term

3.1. Realizability conditions

In the RANS approach, the ensemble average process confines the turbulent effects in the Reynolds stresses, $R_{ij} = \langle u'_i u'_j\rangle$; here, u'_i and u'_j refer to the fluctuating components and $\langle u'_i u'_j\rangle$ is the time-averaged quantity of their product. Therefore, since the averaging operator is a statistical mean, R_{ij} must be symmetric and positive semi-definite in order to ensure physically plausible values, i.e., non-negative real energies. This requirement is equivalent to the conditions of realizability [35] given by the following inequalities[1]

$$R_{\alpha\alpha} \geq 0 \quad \text{for} \quad \alpha \in \{1, 2, 3\}, \tag{8}$$

$$R_{\alpha\beta}^2 \leq R_{\alpha\alpha}R_{\beta\beta} \quad \text{for} \quad \alpha \neq \beta, \tag{9}$$

$$\det(R_{ij}) \geq 0, \tag{10}$$

[1]The summation convention is adopted for Latin, but not for Greek indices.

which guarantee that the spectrum of R_{ij} is non-negative and real.

In a LES context, the common premise is that realizability conditions apply to τ_{ij}. However, rather than a physical requirement, this assumption is a modeling choice to restrict the closure space to non-negative real τ^{sgs}_{kk}. In fact, it has been demonstrated [36] that the conditions are not satisfied for τ_{ij} if nonpositive filters are used. The most general requirement is that the divergence of the filtered advection term is real, i.e., $\partial(\overline{u_i u_j})/\partial x_j \in \mathbb{R}^3$, but this leads to stresses defined up to a constant, and therefore there is no possibility of constructing formal bounds. As a consequence, the approach chosen in this work is to impose realizability conditions to $\overline{u_i u_j} = \overline{u}_i \overline{u}_j + \tau^{sgs}_{ij}$, viz. total filtered energy is non-negative and real, which is a compromise between generality and feasibility. In this regard, the conditions of realizability applied to $\overline{u_i u_j}$ read

$$\overline{u_\alpha u_\alpha} \geq 0 \quad \text{for} \quad \alpha \in \{1,2,3\}, \tag{11}$$

$$\overline{u_\alpha u_\beta}^2 \leq \overline{u_\alpha u_\alpha}\,\overline{u_\beta u_\beta} \quad \text{for} \quad \alpha \neq \beta, \tag{12}$$

$$\det(\overline{u_i u_j}) \geq 0. \tag{13}$$

3.2. Tensor decomposition

The nonlinear filtered advection term can be decomposed into factors by introducing the normalized anisotropy tensor, $\overline{a}_{ij}$, as

$$\overline{a}_{ij} = \frac{\overline{u_i u_j}}{\overline{u_k u_k}} - \frac{1}{3}\delta_{ij} = \overline{v}_{in}\overline{\Lambda}_{nl}\overline{v}_{jl}, \tag{14}$$

which is symmetric and trace-free, i.e., the eigenvalues sum zero. Moreover, its eigendecomposition is given by a matrix of orthonormal eigenvectors, $\overline{v}_{in}$, and a diagonal matrix of eigenvalues, $\overline{\Lambda}_{nl}$, ordered such that $\overline{\lambda}_1 \geq \overline{\lambda}_2 \geq \overline{\lambda}_3$.

The realizability constraints, Eqs. 11-13, bound the intervals of the anisotropy tensor components. The diagonal elements, $\overline{a}_{\alpha\alpha}$, take minimum and maximum values if $\overline{u_\alpha u_\alpha} = 0$ and $\overline{u_\alpha u_\alpha} = \overline{u_k u_k}$, respectively, while, due to the positive semi-definiteness of $\overline{u_i u_j}$, the off-diagonal components, $\overline{a}_{\alpha\beta}$, reach their minimum and maximum values when $\overline{u_\alpha u_\beta} = \pm\overline{u_k u_k}/2$. Introducing these conditions in Eq. 14 results in the following intervals

$$-1/3 \leq \overline{a}_{\alpha\alpha} \leq 2/3 \quad \text{for} \quad \alpha \in \{1,2,3\}, \tag{15}$$

$$-1/2 \leq \overline{a}_{\alpha\beta} \leq 1/2 \quad \text{for} \quad \alpha \neq \beta. \tag{16}$$

Finally, the anisotropy tensor allows reformulating $\overline{u_i u_j}$ in terms of magnitude, $\overline{u_k u_k}$, shape, $\overline{\Lambda}_{nl}$, and orientation, $\overline{v}_{in}$, in the form

$$\overline{u_i u_j} = \overline{u_k u_k}\left(\overline{v}_{in}\overline{\Lambda}_{nl}\overline{v}_{jl} + \frac{1}{3}\delta_{ij}\right). \tag{17}$$

3.3. The barycentric map

For any anisotropy tensor, the diagonal matrix of eigenvalues characterizes the shape of a corresponding ellipsoid. Its major, medium and minor axes compose the basis of eigenvectors, with scalings equal to the values of the associated eigenvalues. The number of non-zero values, i.e., the rank, holds a direct connection with the limiting states of componentiality. In this work, componentiality primarily indicates the number of proper vectors of $\overline{u_i u_j}$ with non-zero scaling, but it can also be utilized to reflect the number of non-zero eigenvalues in the main directions of its resolved, $\overline{u}_i\overline{u}_j$, and modeled parts, τ^{sgs}_{ij}, or in the principal axes of the Reynolds stresses, R_{ij}.

Three limiting shapes exist in the case of a positive semi-definite second-order tensor. The one-component limiting state (rod-like) corresponds to a one-rank tensor where $2/3 = \lambda_1 > \lambda_2 = \lambda_3 = -1/3$. Similarly, the two-component axisymmetric limiting state (disk-like) presents two principal directions with equal non-zero eigenvalues of value $1/6 = \lambda_1 = \lambda_2 < \lambda_3 = -1/3$. Finally, the three-component isotropic limiting state (spherical) is characterized by a basis of eigenvectors with all eigenvalues equal to zero, i.e., $\lambda_1 = \lambda_2 = \lambda_3 = 0$.

Tensor anisotropy, or shape, is usually visualized by means of anisotropy-invariant maps (AIM). In the context of turbulence analysis, commom AIMs are the nonlinear Lumley [37] and turbulence [38] triangles or the linear eigenvalue map [37]. An alternative construction is the barycentric map [39]. This approach relies on the fact that any anisotropy state is a convex combination of the limiting states of componentiality. In an Euclidean space, these can be represented, for example, as the vertices of an equilateral triangle with coordinates $\mathbf{x}_{1c} = (0,0)$, $\mathbf{x}_{2c} = (1,0)$, and

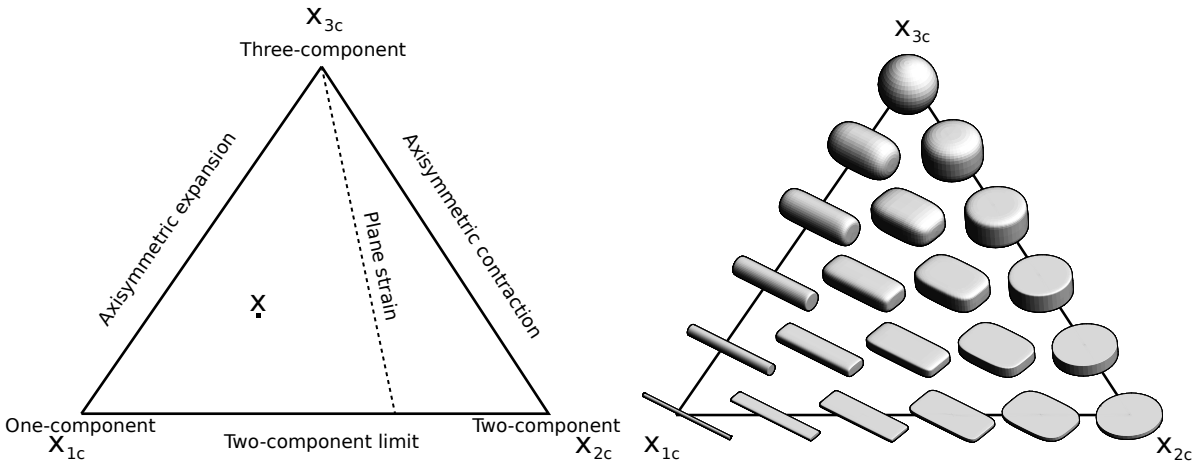

Figure 1: Barycentric map based on the eigenvalues of a general second-order anisotropy tensor. Left: limiting states of componentiality. Right: tensor shapes visualized with superquadric glyphs [40] (figure regenerated using open-source software [41]).

$\mathbf{x}_{3c} = (1/2, \sqrt{3}/2)$. A graphical representation of the map and the different anisotropy shapes is illustrated in Fig. 1. One of the main advantages is that it provides a linear relation between anisotropy eigenvalues and Euclidean space through the projection

$$\mathbf{x} = \mathbf{x}_{1c}\,(\lambda_1 - \lambda_2) + 2\mathbf{x}_{2c}\,(\lambda_2 - \lambda_3) + \mathbf{x}_{3c}\,(3\lambda_3 + 1)\,. \tag{18}$$

This projection, together with the requirement that the eigenvalues sum zero, is a unique invertible linear mapping that can be mathematically expressed as $x_i = B_{in}\Lambda_{nl}$. Note that realizability conditions imply that any anisotropy state of $\overline{u_i u_j}$ lies within the triangle (indicated in Fig. 2 by $\overline{\mathbf{x}}$).

4. Structural uncertainty estimation framework

The strategy to analyze model-form error in the underlying SGS closure is to introduce controlled perturbations into the nonlinear filtered advection term such that their impact on the QoI can be assessed. In a LES context, large scales are directly resolved, whereas model assumptions are confined to the subgrid scales. Consequently, in order to restrict the injection to τ_{ij}^{sgs}, the decomposed $\overline{u_i u_j}$, Eq. (17), needs to be separated into resolved and modeled parts. This is accomplished through the following expression

$$\overline{u_i u_j} = \overline{u_k u_k}\left(a_{ij}^{res} + a_{ij}^{sgs} + \frac{1}{3}\delta_{ij}\right), \tag{19}$$

where a_{ij}^{res} and a_{ij}^{sgs} are the resolved and SGS components of the total anisotropy tensor given by

$$a_{ij}^{res} = \frac{1}{\overline{u_k u_k}}\left(\overline{u}_i\overline{u}_j - \frac{\overline{u}_k\overline{u}_k}{3}\delta_{ij}\right) = v_{in}^{res}\Lambda_{nl}^{res}v_{jl}^{res} \quad \text{and} \quad a_{ij}^{sgs} = \frac{1}{\overline{u_k u_k}}\left(\tau_{ij}^{sgs} - \frac{\tau_{kk}^{sgs}}{3}\delta_{ij}\right) = v_{in}^{sgs}\Lambda_{nl}^{sgs}v_{jl}^{sgs}, \tag{20}$$

with $\overline{u}_k\overline{u}_k$ the resolved part of $\overline{u_k u_k}$.

Once the separation between resolved and modeled parts is performed, perturbations are defined as

$$\overline{u_i u_j}^{*} = \overline{u}_i\overline{u}_j + \tau_{ij}^{sgs*} = \overline{u}_i\overline{u}_j + \overline{u_k u_k}^{*}a_{ij}^{sgs*} + \frac{\tau_{kk}^{sgs*}}{3}\delta_{ij}, \tag{21}$$

$$\text{with} \quad \overline{u_k u_k}^{*} = \overline{u}_k\overline{u}_k + \tau_{kk}^{sgs*} \quad \text{and} \quad a_{ij}^{sgs*} = v_{in}^{sgs*}\Lambda_{nl}^{sgs*}v_{jl}^{sgs*}. \tag{22}$$

Thus, perturbations (indicated with *) are applied to the subgrid-scales only, and are specified as a discrepancy of the SGS tensor in terms of magnitude ($\tau_{kk}^{sgs*} = \tau_{kk}^{sgs} + \Delta\tau_{kk}^{sgs}$), shape (diagonal matrix Λ_{nl}^{sgs*} of perturbed eigenvalues λ_l^*), and orientation ($v_{ij}^{sgs*} = q_{in}v_{nj}^{sgs}$ with q_{in} an orthonormal rotation matrix).

4.1. Modeled subgrid-scale tensor magnitude perturbation

Lower and upper bounds for the perturbation of τ_{kk}^{sgs} can be obtained by considering the sign nature of the quantities composing the trace of the nonlinear filtered advection term. Its mathematical expression is

$$\overline{u_k u_k} = \overline{u}_k \overline{u}_k + \tau_{kk}^{sgs}, \tag{23}$$

where $\overline{u_k u_k}$ and $\overline{u}_k \overline{u}_k$ are non-negative. The former, $\overline{u_k u_k}$, is non-negative due to the restriction made in this work that realizability conditions apply to $\overline{u_i u_j}$, whereas the latter, $\overline{u}_k \overline{u}_k$, is non-negative by construction independently of the filter utilized, given its square product expression. In order to respect these properties, any possible perturbation of τ_{kk}^{sgs} is bounded by $\overline{u_k u_k} = \overline{u}_k \overline{u}_k + \tau_{kk}^{sgs} \geq 0$ and $\overline{u}_k \overline{u}_k = \overline{u_k u_k} - \tau_{kk}^{sgs} \geq 0$. Therefore, the interval of magnitude discrepancy written in terms of $\Delta\tau_{kk}^{sgs}$ results in

$$-\overline{u}_k \overline{u}_k - \tau_{kk}^{sgs} \leq \Delta\tau_{kk}^{sgs} \leq \overline{u_k u_k} - \tau_{kk}^{sgs}. \tag{24}$$

Notice that expressions for $\overline{u_k u_k}$ and τ_{kk}^{sgs} are not typically considered in LES calculations. The latter is absorbed in the pressure term for incompressible flow, while commonly considered small for low-Mach-number and compressible flows. However, closures for its evaluation exist in the literature; for instance, the model proposed by Yoshizawa [33]. On the other hand, $\overline{u_k u_k}$ is always decomposed into resolved and modeled parts, and consequently is never explicitly computed. Even so, deconvolution methods [42] are frequently utilized to approximate the subfilter velocity, $u_i{}'$, of the Navier-Stokes equations. To a first approximation, similar approaches could be applied to directly model $\overline{u_k u_k}$.

4.2. Modeled subgrid-scale tensor eigenvalue perturbation

Different strategies can be designed to perturb the eigenvalues of a_{ij}^{sgs}. In fact, the framework proposed allows the perturbations to be defined implicitly through the coordinates in the barycentric map as $\lambda_l^{sgs*} = \mathbf{B}^{-1}\mathbf{x}^{sgs*}$ independently of their nature. For this initial study, we choose the uncertainty to be characterized by a direction, $\mathbf{x}^t - \mathbf{x}^{sgs}$, and a magnitude, $|\mathbf{x}^t - \mathbf{x}^{sgs}|$, both of which could vary in space and time. In particular, perturbations within the barycentric map are considered toward each of the three corners of the triangle, namely $\mathbf{x}_{1c}$, $\mathbf{x}_{2c}$, and $\mathbf{x}_{3c}$, and are defined by means of a relative distance Δ_B toward the target vertex. In mathematical form, the eigenvalue perturbation can be expressed through the following translation

$$\mathbf{x}^{sgs*} = \mathbf{x}^{sgs} + \Delta_B \left(\mathbf{x}^t - \mathbf{x}^{sgs} \right), \tag{25}$$

where $\mathbf{x}^{sgs}$, $\mathbf{x}^{sgs*}$, and $\mathbf{x}^t$ are the coordinates of the base-model prediction, new pertubed position and target corner, respectively. This translation process is illustrated in Section 4.2.1. Finally, by applying the linear map $\mathbf{B}$ to the new position $\mathbf{x}^{sgs*}$, the perturbed eigenvalues are uniquely defined as

$$\lambda_l^{sgs*} = (1 - \Delta_B)\, \lambda_l^{sgs} + \Delta_B \lambda_l^t. \tag{26}$$

4.2.1. Graphical representation

Injection of shape uncertainty into the modeled part of $\overline{u_i u_j}$ is represented in Fig. 2. First, the eigenvalues of the resolved and SGS base-model tensors determine the initial location of $\overline{a}_{ij}$ in the map, $\overline{\mathbf{x}}$. Note that $\overline{\mathbf{x}}$ is not a direct summation of $\mathbf{x}^{res}$ and $\mathbf{x}^{sgs}$ since the eigenvectors of the tensors are, in general, different. In particular, this example depicts the case in which the shape of a_{ij}^{res} is predominantly rod-like, and the SGS tensor is approximated by an eddy-viscosity-type model. Subsequently, uncertainty is introduced by applying a translation to $\mathbf{x}^{sgs}$ of magnitude Δ_B toward $\mathbf{x}^t$ ($\mathbf{x}_{2c}$ in this example), resulting in the perturbed location $\mathbf{x}^{sgs*}$. Finally, the perturbation to the eigenvalues of the SGS part, together with the contribution from the resolved scales, induces a new location within the barycentric map indicated as $\overline{\mathbf{x}}^*$.

4.3. Modeled subgrid-scale tensor eigenvector perturbation

The methodology to introduce perturbations into the eigenvectors of a_{ij}^{sgs} is based on the physical constraints of energy transfer between resolved and modeled scales. The starting point is the balance equation for resolved filtered kinetic energy, $E_f = \overline{u}_k \overline{u}_k / 2$, given as [43]

$$\frac{\partial E_f}{\partial t} + \overline{u}_j \frac{\partial E_f}{\partial x_j} - \frac{\partial}{\partial x_i} \left[\overline{u}_j \left(2\nu \overline{S}_{ij} - \tau_{ij} - \frac{1}{\rho} \overline{p}\, \delta_{ij} \right) \right] = -\epsilon_f - \mathcal{P}_r. \tag{27}$$

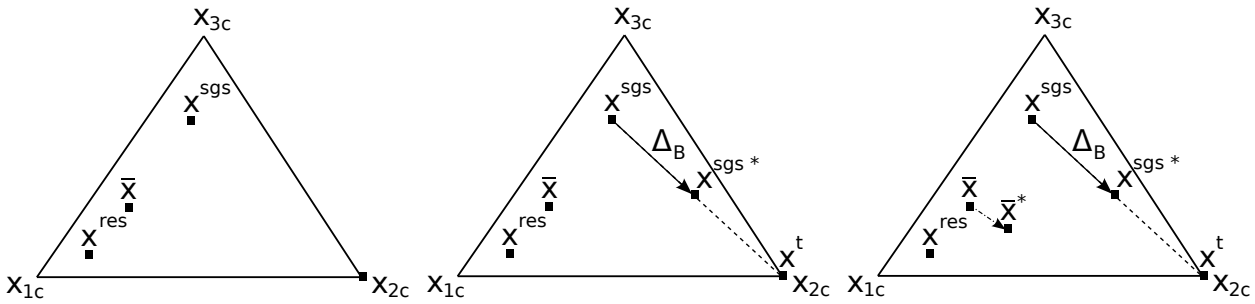

Figure 2: Sequential illustration of the eigenvalue perturbation procedure. The resolved, $\mathbf{x}^{res}$, and SGS base-model, $\mathbf{x}^{sgs}$, parts provide an initial location $\overline{\mathbf{x}}$ within the triangle (left). A perturbation of magnitude Δ_B toward $\mathbf{x}_{2c}$ is applied to $\mathbf{x}^{sgs}$ (center). The new location of the SGS part, $\mathbf{x}^{sgs*}$, indirectly modifies the coordinates of $\overline{\mathbf{x}}$, resulting in a perturbed state $\overline{\mathbf{x}}^*$ (right).

The terms on the left-hand side represent transport, while the terms on the right-hand side correspond to viscous dissipation, $\epsilon_f = 2\nu\overline{S}_{ij}\overline{S}_{ij}$, and rate of production of SGS kinetic energy, $\mathcal{P}_r = -\tau_{ij}\overline{S}_{ij}$. The latter is of particular interest since it represents the transfer of energy between resolved and modeled scales. In three-dimensional (3-D) turbulence, $\mathcal{P}_r$ transfers energy from large to small scales in a statistically-averaged sense, i.e., forward-scatter. However, it can present positive or negative values instantaneously, and therefore it can act as a sink (forward-scatter) or source (backscatter) term for E_f [44].

In the above equation, the transport of SGS stresses, $\partial(\overline{u}_j\tau_{ij})/\partial x_i$, and $\mathcal{P}_r$ require closure through τ_{ij}. However, modeling $\partial(\overline{u}_j\tau_{ij})/\partial x_i$ involves non-local information due to the differentiation operator. By contrast, it is reasonable to consider the modeling of $\mathcal{P}_r$ local since τ_{ij}^{sgs} is typically closed based on local information. The SGS kinetic energy production rate term is an inner product between τ_{ij} and $\overline{S}_{ij}$ equal to $\mathcal{P}_r = -\text{tr}(\tau_{ij}\overline{S}_{ij})$. In this regard, the value of the inner product depends on the alignment between the eigenvectors of τ_{ij} and $\overline{S}_{ij}$. Diverse alignments between these two tensors can be considered. However, for the purpose of enveloping the possible dynamics, the methodology proposed seeks the extremal values of this inner product. In the case of τ_{ij} being real and $\overline{S}_{ij}$ real symmetric, the lower and upper bounds are given by the following expression [45]

$$\lambda_1\gamma_3 + \lambda_2\gamma_2 + \lambda_3\gamma_1 \leq \mathcal{P}_r \leq \lambda_1\gamma_1 + \lambda_2\gamma_2 + \lambda_3\gamma_3, \tag{28}$$

with λ_l and γ_l the eigenvalues of τ_{ij} and $\overline{S}_{ij}$, respectively. The upper bound in this inequality corresponds to the situation in which τ_{ij} and $\overline{S}_{ij}$ share the same basis of eigenvectors, while the lower bound is the case in which the eigenvector bases are the same except for a permutation between the first and third eigenvectors. From a practical point of view, the existence of bounds suggests that only two eigenvector sets need to be considered. These can be easily analyzed by setting the perturbed eigenvectors of τ_{ij}^{sgs} to be the eigenvectors of $\overline{S}_{ij}$ with and without a permutation of its first and third eigenvectors.

Caution is required, however, when considering the case with permuted eigenvectors. Its negative character introduces backscatter into the discrete system and may result in unstable computations as kinetic energy will tend to accumulate at the grid scale [46]. In this regard, if perturbations vary in time and space, the only necessary requirement is to satisfy the second law of thermodynamics, viz. the net transport of energy is of forward-scatter type. On the contrary, if perturbations are constant in space and time, one possible local constraint is to impose the perturbed SGS kinetic energy production rate term to be smaller in magnitude than the viscous dissipation, i.e., $|\mathcal{P}_r| \leq 2\nu\text{tr}(\overline{S}_{ij}^2)$, by setting the instantaneous turbulent viscosity to be $\nu_{sgs} \leq \nu$.

5. Numerical experiments

The performance of the structural UQ framework proposed is investigated by computing LES of turbulent flow with the unstructured and massively parallel Nalu open-source code [47]. First, sensitivity to injection of individual homogeneous perturbations in the magnitude, anisotropy and orientation of the modeled SGS tensor is carefully

analyzed. Subsequently, the methodology is applied within a (small) ensemble calculation in which combined perturbations are considered. In this section, results corresponding to the WALE model [29] (eddy-viscosity-type family) without perturbations are referred to as base-model solutions, while computations where magnitude, shape or orientation uncertainty has been introduced are designated by the sign of magnitude discrepancy ($\Delta\tau_{kk}^{sgs} < 0$ or $\Delta\tau_{kk}^{sgs} > 0$), target corner (1-comp., 2-comp., or 3-comp.) or eigenvector permutation (perm. 1, perm. 2, or perm. 3) of the respective perturbation.

The canonical periodic channel flow at friction Reynolds number $Re_\tau = 395$ is selected as test case; numerical results will be compared to reference DNS data from Moser et al. [48]. As is customary, $Re_\tau = u_\tau h/\nu$ with u_τ being the friction velocity, h the channel half-height, and ν the kinematic velocity of the fluid. The mass flow rate is determined through a static pressure gradient $dp/dx = -\tau_w/h$, where τ_w is the wall shear stress. The computational domain is $2\pi h \times 2h \times \pi h$ in the streamwise (x), vertical (y), and spanwise (z) directions, respectively. Streamwise and spanwise boundaries are set periodic, and no-slip conditions are imposed to the horizontal boundaries (x-z planes). The grid is uniform in the streamwise and spanwise directions with spacings in wall units equal to $\Delta x^+ = 38.8$ and $\Delta z^+ = 12.9$, while stretched in the vertical direction with the first grid point at $y^+ = 0.5$ and with resolutions in the range $\Delta y^+ = [0.5 - 15.1]$. This grid arrangement corresponds to a wall-resolved LES of size $64 \times 128 \times 96$. The simulations start from a sinusoidal velocity field from which turbulence develops and reaches steady-state behavior after several flow through times. For each calculation, the averaging process is started once a sufficiently long transient period is surpassed (approximately at $t = 100h/u_\tau$), and statistics are collected over a time interval of length $T = 1000h/u_\tau$.

5.1. Sensitivity analysis of individual uncertainties

Individual perturbations to the magnitude (τ_{kk}^{sgs}), shape (Λ_{nl}^{sgs}), and orientation (v_{in}^{sgs}) of the SGS stress tensor are considered first in order to estimate their isolated effects on the QoIs. In detail, magnitude perturbations are discussed in Sec. 5.1.1, shape perturbations in Sec. 5.1.2, and orientation permutations in Sec. 5.1.3. For each type of uncertainty, perturbations are fully described and their effects carefully interpreted by extracting the physical mechanisms responsible for deviations from the base-model prediction. In addition, connections between the different perturbations are exposed to further understand their similarities and differences. Finally, the insight gained from this analysis is later leveraged in Sec. 5.2 to characterize the limiting values of the perturbation parameters for a batch of samples.

5.1.1. Uncertainty in tensor magnitude

The effects of structural uncertainty in the magnitude of the SGS stress tensor are estimated by applying perturbations to the base-model τ_{kk}^{sgs} value. Two opposite cases are studied based on the limits of Eq. 24. In one the tensor magnitude is augmented by setting the perturbation to $\Delta\tau_{kk}^{sgs} = \overline{u_k u_k} - \tau_{kk}^{sgs}$ ($\Delta\tau_{kk}^{sgs} > 0$), while in the other the discrepancy is set to $\Delta\tau_{kk}^{sgs} = -\overline{u}_k\overline{u}_k - \tau_{kk}^{sgs}$ ($\Delta\tau_{kk}^{sgs} < 0$). These two extreme cases can be roughly interpreted as multiplying the turbulent viscosity by two and switching the SGS model off, respectively.

The prediction of averaged (in time and x- and z-directions) streamwise velocity obtained from the base-model and perturbed LES calculations is shown in Fig. 3(a). An important observation is that the combination of mesh and base-model chosen for the numerical experiments provides results in good agreement with the DNS solution. This feature is not a mere coincidence, it is in fact a desired requirement for these calculations; different spatial discretizations have been explored for this purpose as detailed in the Appendix. Consistency with DNS data is a choice made to present the results since the objective is not to develop a more accurate SGS model, but to introduce a framework to study sensitivity to model-form uncertainty. In particular, we are interested in exploring the performance of the methodology in the context of predictive studies for which fairly well-resolved LES are expected.

The effect of discrepancy in tensor uncertainty on averaged streamwise velocity is better visualized in Fig. 3(b), where the normalized relative difference of the perturbed LES solutions with respect to the base-model prediction is plotted. Differences in the viscous sublayer are practically negligible due to the inherent construction of the base-model which tends to zero in near-wall regions (cubic behavior [49] designed to mimic turbulence damping due to no-slip boundary conditions), and therefore both the base and perturbed LES models are in practice switched off. However, in the buffer layer and log-law region, where the contribution from the LES models becomes important, enlarging or shrinking the size of the SGS stresses results in two opposite behaviors. For $\Delta\tau_{kk}^{sgs} < 0$, the averaged streamwise velocity is decreased by a relative factor of 0.02, while symmetrically increased for $\Delta\tau_{kk}^{sgs} > 0$. For eddy-viscosity-type closures, like the base-model chosen in this work, this trend can be understood from SGS kinetic

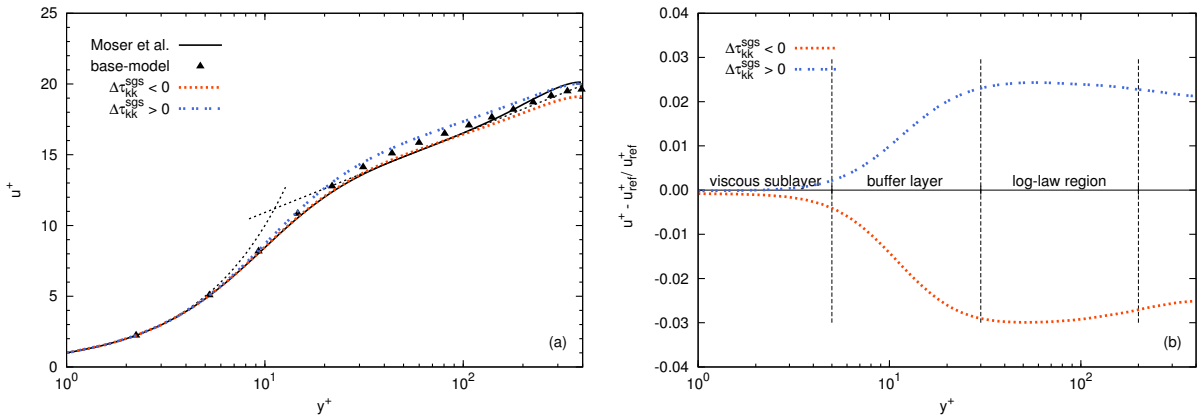

Figure 3: Effect of SGS stress tensor magnitude perturbation on averaged streamwise velocity (quantities in wall units). (a) y-axis profiles of DNS data from [48] (solid line), base-model solution (solid triangles), and magnitude perturbation results (dashed lines). (b) Normalized relative difference with respect to base-model prediction.

energy considerations as perturbations in magnitude can be directly interpreted as $\mathcal{P}_r^* = 2\nu_{sgs}^* \mathrm{tr}(\overline{S}_{ij}^2)$. Consequently, increasing the magnitude of τ_{ij}^{sgs} reduces the amount of kinetic energy in the system, which accordingly results in a more parabolic-like streamwise velocity profile. The opposite effect is obtained for $\Delta\tau_{kk}^{sgs} < 0$, since SGS kinetic energy dissipation is reduced and the profile becomes flatter due to an increase in turbulence levels.

As it is deduced from the plots, the effects of magnitude perturbation on the flow field are rather small, especially when compared to discrepancies in anisotropy or orientation as it will be shown below. The main reason for the limited effects is the small values of ν_{sgs} with respect to the fluid kinematic viscosity; for example, the ratio is $\langle\nu_{sgs}\rangle/\nu < 0.4$ for the base-model case. This is a direct consequence of the relatively fine mesh chosen in this study, but exposes the small range of deviations in QoI prediction that a set of different eddy-viscosity models can provide as they only account for variations in tensor magnitude.

5.1.2. Uncertainty in tensor anisotropy

Model-form uncertainty in the spectrum of τ_{ij}^{sgs} is analyzed by perturbing the eigenvalues of the base-model tensor. Three cases are considered in which the anisotropy of the SGS tensor is forced toward the limiting states of the barycentric map. As described in Section 4.2, these cases correspond to perturbations toward the one-component (1-comp.), two-component (2-comp.), and three-component (3-comp.) vertices of the triangle. The perturbation distances are chosen to be $\Delta_B = 0.001$, 0.001 and 1.0, respectively. In a relative sense, these magnitudes are small for cases 1- and 2-comp. in comparison to case 3-comp. However, these values are not directly representative of the perturbations with respect to the size of τ_{ij}^{sgs}. The SGS anisotropy tensor in Eq. 20 is normalized by $\overline{u_k u_k}$. Under this normalization, the eigenvalues obtained from the eigendecomposition are small, and therefore their location on the barycentric map is close to the $\mathbf{x}_{3c}$ vertex as depicted in Fig. 4. As a consequence, perturbations toward vertices $\mathbf{x}_{1c}$ or $\mathbf{x}_{2c}$, although small in relative value, are large in absolute terms. It is important to highlight that this initial location of the SGS base-model eigenvalues on the barycentric map does not restrict Δ_B from taking values close to 1 for perturbations toward $\mathbf{x}_{1c}$ or $\mathbf{x}_{2c}$. In fact, numerical experiments with $\Delta_B \sim 1$ for cases 1- and 2-comp. have been conducted. For the channel flow problem, however, the fact that perturbations are spatially uniform in the presence of periodic boundaries results in an excessive accumulation of the perturbation effects after several flow through times, and therefore results are shown in this work for the Δ_B values given above.

The effects of perturbing the eigenvalues of the SGS stress tensor are shown in Fig. 5 for the averaged streamwise velocity profile (a) and rms velocity fluctuations (b, c, d). Deviations from the base-model prediction are larger than in the case of perturbing the magnitude of the SGS stresses. This result is relevant as it demonstrates the importance of considering variations in all the degrees of freedom. For instance, an ensemble calculation in which different eddy-viscosity models are utilized would not have been able to capture the larger variability on the QoIs that the SGS stresses inherently possess. In terms of averaged streamwise velocity, Fig. 5(a) shows that perturbations to the

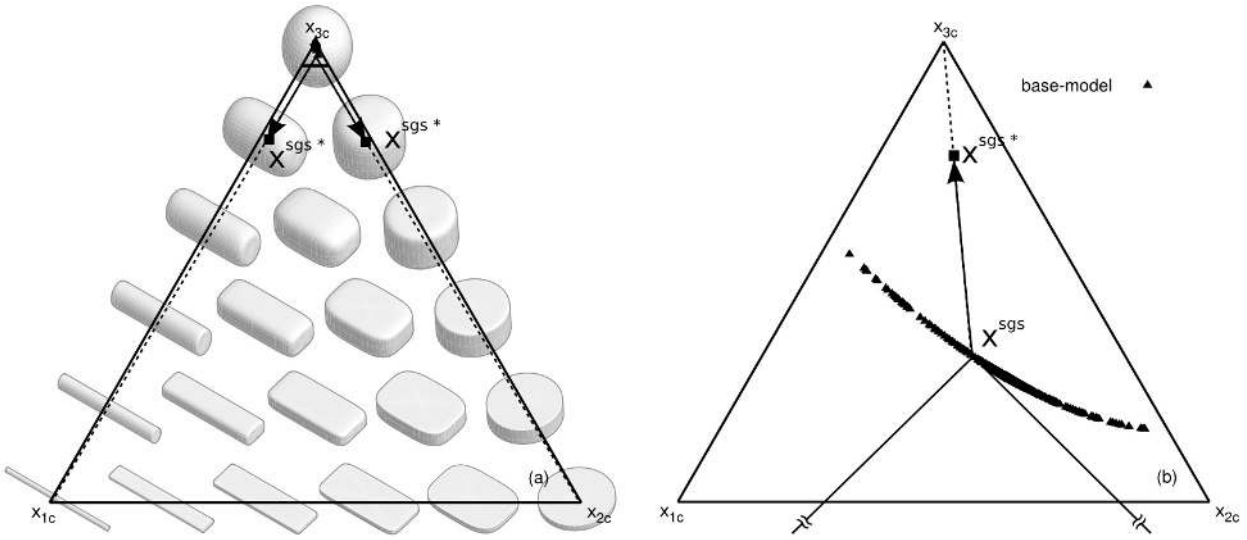

Figure 4: Representation on the barycentric map of instantaneous SGS base-model tensor anisotropies (solid triangles). Examples of eigenvalue perturbation to the three vertices of the triangle are schematically illustrated. (a) SGS stress anisotropy tensor normalized by $\overline{u_k u_k}$. (b) SGS stress anisotropy tensor normalized by τ_{kk}^{sgs} based on Yoshizawa's model [33].

anisotropy of τ_{ij}^{sgs} results in a bounding interval. In particular at $y^+ = Re_\tau$, the solution interval is limited by the 1- and 3-comp. perturbations with values $u^+ = 23.6$ and 19.1, respectively, and which effectively envelope the base-model prediction ($u^+ = 19.6$) and DNS result ($u^+ = 20.1$). The outcome of eigenvalue perturbation is better comprehended by considering the average profiles of rms velocity fluctuations plotted in Fig. 5(b, c, d). In comparison to the base-model solution, forcing τ_{ij}^{sgs} to be more rod-like reduces the velocity fluctuations in the vertical and spanwise directions of the flow, while increases their magnitude in the streamwise dimension. This combination results in an overall laminarization of the flow, and consequently the mass flow rate for a given static pressure gradient is increased as captured by the averaged velocity profile. Similarly, perturbations toward the two-component vertex (2-comp.) result in a deviation of the fluctuations from the base-model solution to a more disk-like configuration; fluctuation intensities are largely reduced for v_{rms}^+ and w_{rms}^+ in comparison to u_{rms}^+. By contrast, the effects of perturbing toward the isotropic limiting state are very small. For instance, the streamwise velocity barely deviates from the base-model prediction. Finally, to further illustrate the perturbation effects, contours of instantaneous streamwise velocity for the 1-comp. case are qualitatively compared to the base-model solution in Fig. 6. Taking as a reference the base-model velocity field (top row), perturbing toward the one-component limiting state (center row) results in a reduction in turbulence intensity levels (flow laminarization), especially at the centerline region of the channel where the SGS model is active.

5.1.3. Uncertainty in tensor orientation

Propagation of incertitude in the orientation of the modeled SGS stress tensor is studied by constructing τ_{ij}^{sgs} based on rearrangements of the eigenvectors of $\overline{S}_{ij}$. As discussed in Section 4.3, two limiting states of eigenvector perturbation seem *a priori* good candidates. However, three cases are considered for completeness. The first permutation (perm. 1) sets the eigenvectors of τ_{ij}^{sgs} directly equal to the proper basis of $\overline{S}_{ij}$; this permutation is equivalent to the base-model in the absence of perturbations, and is reported here as a reference. The third permutation is exactly equal to perm. 1, but with a shift between the first and third eigenvectors. Finally, the second permutation (perm. 2) is an intermediate case in which the second and third eigenvectors of perm. 1 are interchanged. No additional modifications are required except for perm. 3 in which, due to the sustained introduction of kinetic energy from the SGS to the resolved scales (backscatter), the constraint proposed in Sec. 4.3 is imposed on the magnitude of τ_{ij}^{sgs} to ensure that viscous forces are able to locally dissipate sufficient SGS kinetic energy to maintain the calculation stable.

Variations in averaged streamwise velocity due to the three eigenvector perturbations are plotted in Fig. 7(a), together with the base-model and DNS solutions. The first observation is that the two limiting candidates proposed

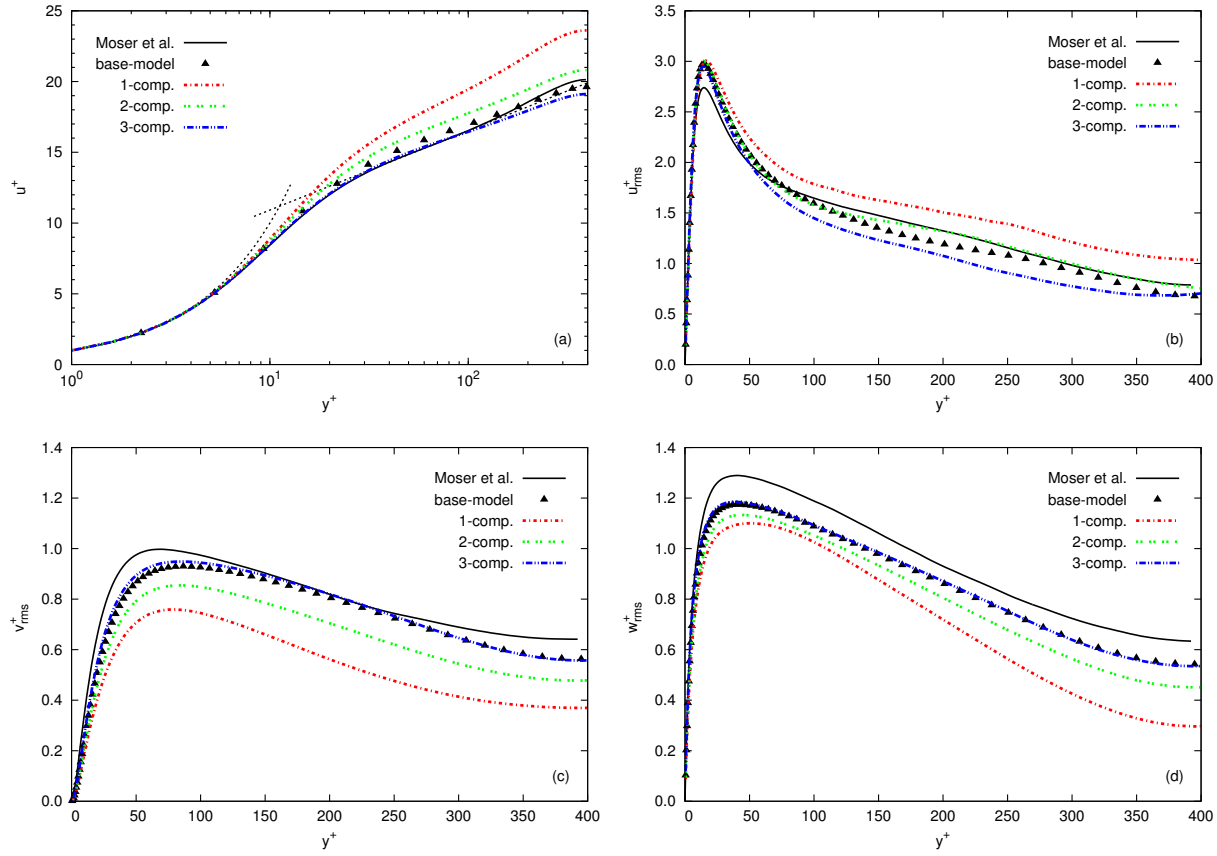

Figure 5: Effects of SGS stress tensor eigenvalue perturbation (quantities in wall units). (a) Averaged streamwise velocity profile. (b) Streamwise rms velocity fluctuation. (c) Vertical rms velocity fluctuation. (d) Spanwise rms velocity fluctuation. DNS data from [48] (solid line), base-model solution (solid triangles), eigenvalue perturbation results (dashed lines).

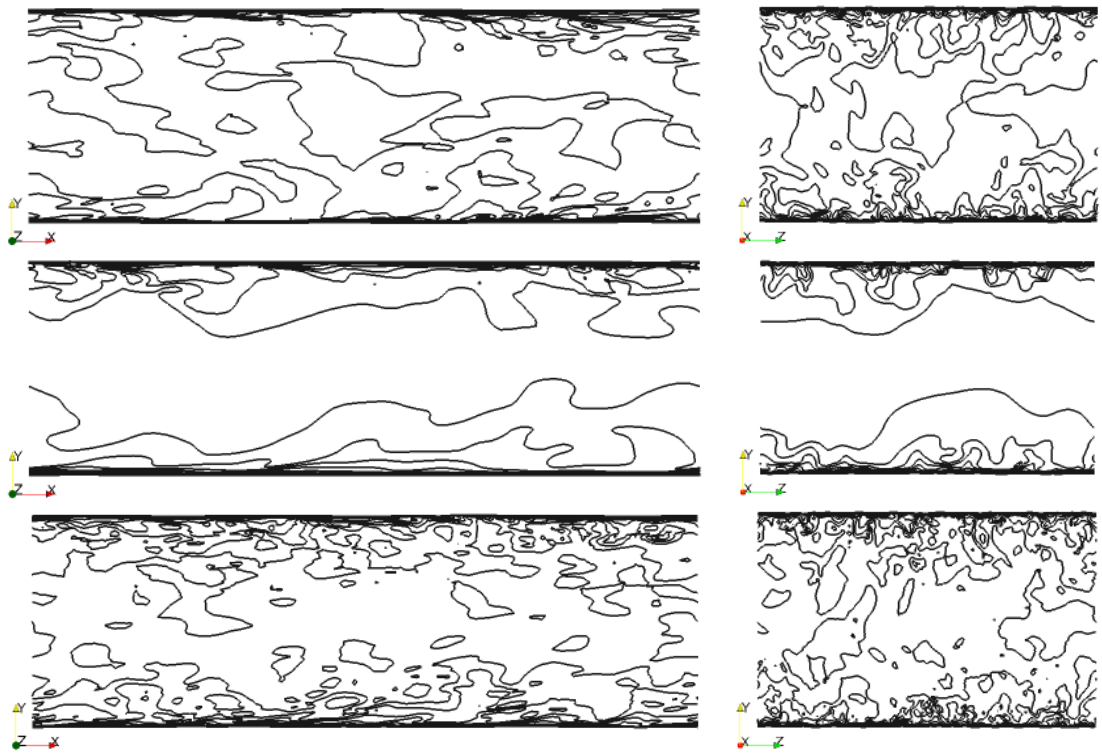

Figure 6: Effect of SGS stress tensor perturbation on instantaneous streamwise velocity (contours). Base-model (top), 1-comp. eigenvalue perturbation (center), perm. 3 eigenvector perturbation (bottom). Images correspond to the *xy*- (left) and *yz*-plane (right) views.

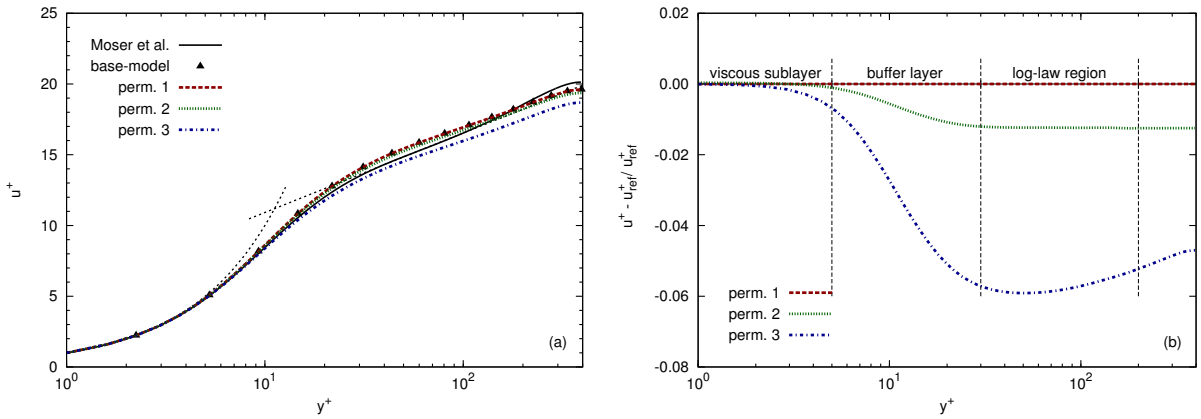

Figure 7: Effect of SGS stress tensor eigenvector perturbation on averaged streamwise velocity (quantities in wall units). (a) y-axis profiles of DNS data from [48] (solid line), base-model solution (solid triangles), and eigenvector perturbation results (dashed lines). (b) Normalized relative difference with respect to base-model prediction.

for enveloping the uncertainty in eigenvector basis are successful, viz. the result of perm. 2 is bounded by the solutions of perm. 1 and perm. 3 as clearly shown in Fig. 7(b). In particular, deviations from the base-model prediction for perm. 3 are two times larger in comparison to the deviations obtained for the perturbations in magnitude. The second observation is that perm. 1 and base-model give the same prediction as expected.

The physical mechanism responsible for the change in averaged streamwise velocity profile is inferred from the transport equation of filtered kinetic energy, Eq. 27. In the case of perm. 1, the orientation of the SGS stress tensor is exactly equal to the eigenvector basis of $\overline{S}_{ij}$. This alignment between tensors forces the inner product $\mathcal{P}_r$ to be defined positive. Consequently, the SGS kinetic energy production rate term acts as a sink extracting energy from the resolved to the modeled scales, and consequently reduces the magnitude of the velocity fluctuations. At the opposite extreme, perm. 3 energizes the flow by setting $\mathcal{P}_r$ to be negative, thereby acting as a source of kinetic energy from the small to the large scales. As a result, the flow becomes more turbulent and the streamwise velocity profile flattens. This description is in accordance with the rms velocity fluctuations depicted in Fig. 8. As it can be observed, the difference in fluctuation intensity between the three spatial dimensions is reduced, especially at the centerline region of the channel. Different magnitude levels in the effects of perm. 3 can be obtained by modifying the constraint required to guarantee that the second law of thermodynamics is satisfied in a statistically-averaged sense. Nonetheless, we find the local condition proposed in this work to be effective as it maintains the calculations numerically stable while allowing for sufficient backscatter such that sensitivity to perm. 3 can be analyzed.

Effects on the orientation of the Reynolds stresses have been considered. Particularly, Rose diagrams of the R_{ij} polar (θ) and azimuthal (ϕ) spherical angles have been computed from the averaged solution of the three permutations. However, the pressure gradient imposed to the flow completely dominates the orientation of the stresses, hiding the smaller effects produced by the perturbations. Of particular interest would be their study in complex flow configurations with inflow-outflow boundary conditions. Lastly, similar to case comp. 1, contours of instantaneous streamwise velocity for perm. 3 are qualitatively contrasted to the base-model solution in Fig. 6. As shown by the contours, perturbation of the SGS stress tensor orientation by means of perm. 3 (bottom row) has a net effect of increasing the magnitude of the velocity fluctuations. In comparison to the base-model prediction, this increase results in more fragmented flow structures which are indicative of solutions presenting higher levels of turbulence.

5.2. Ensemble estimation of combined uncertainties

Estimation of the effects resulting from combining different types of perturbations is the final goal of this work. One option could be to consider pairs of combinations based on the individual limiting cases of the sensitivity analysis. For example, perturbation $\Delta\tau_{kk}^{sgs} > 0$ combined with perm. 3. However, due to the moderate complexity of turbulent channel flow, we can qualitatively anticipate what the effects would be. For the example proposed, perm. 3 would result in injection of energy (backscatter), which would be enhanced due to an increase in tensor magnitude by

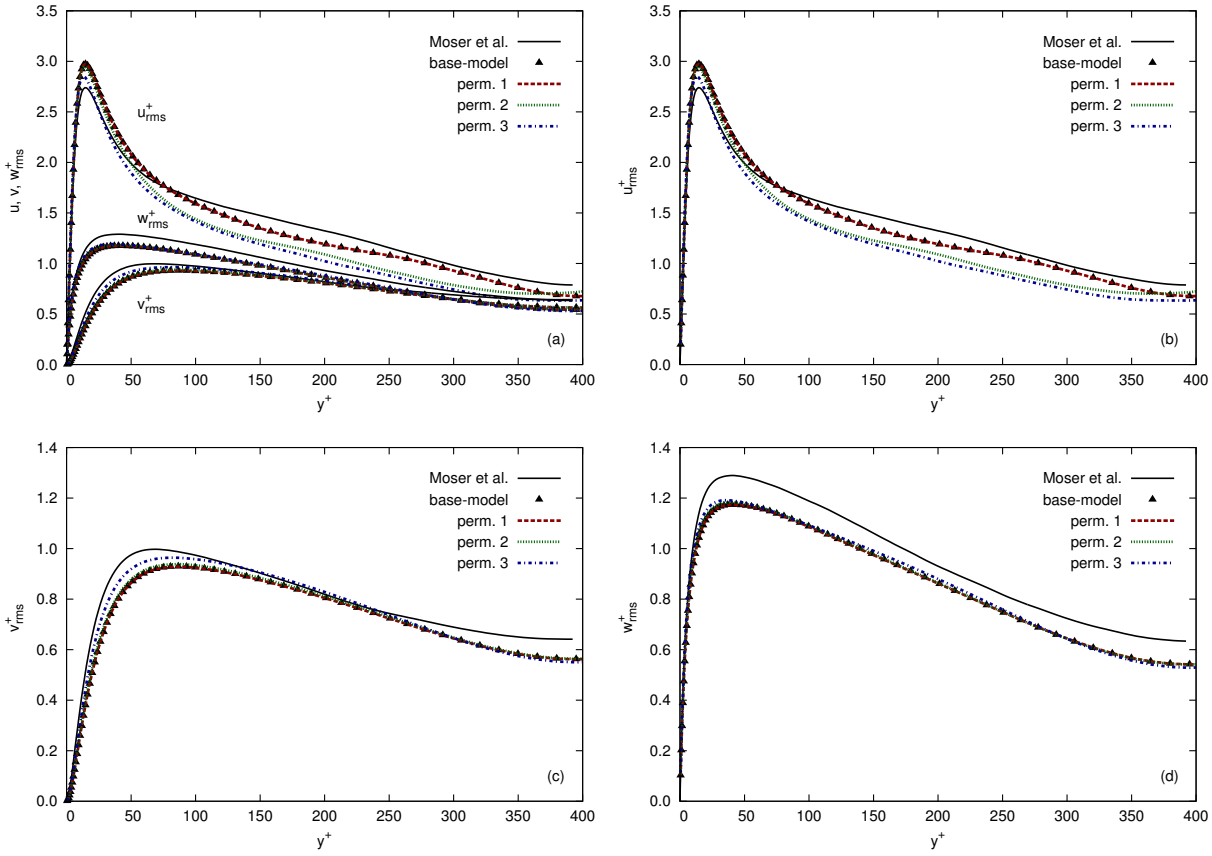

Figure 8: Effects of SGS stress tensor eigenvector perturbation on velocity fluctuations (quantities in wall units). (a) Velocity fluctuations in the principal directions. (b) Streamwise rms velocity fluctuation. (c) Vertical rms velocity fluctuation. (d) Spanwise rms velocity fluctuation. DNS data from [48] (solid line), base-model solution (solid triangles), eigenvector perturbation results (dashed lines).

Sample	1	2	3	4	5	6	7	8
$\Delta\tau_{kk}^{sgs}/\overline{u}_k\overline{u}_k$ (10^{-1})	-0.8	0.5	-7.8	-3.5	0.6	1.4	-4.3	7.1
Δ_B (10^{-4})	8.2	3.3	4.9	4.0	0.4	8.8	5.7	2.4
$\mathbf{x}^t$	2	1	2	1	3	1	3	2
Perm.	1	1	3	3	1	3	3	3

Table 1: Values of the perturbation parameters for the eight samples in the ensemble calculation. Discrepancy in tensor magnitude ($\Delta\tau_{kk}^{sgs}$), relative distance (Δ_B) and target vertex ($\mathbf{x}^t$) of anisotropy uncertainty, and permutation (Perm.) in tensor orientation.

$\Delta\tau_{kk}^{sgs} > 0$. A different approach, which results in different variability, is to analyze the effects of combining random perturbations within a batch of samples. This idea can be interpreted as an ensemble calculation in which, instead of a set of LES models that may be all based on similar physical assumptions and therefore may lead to a biased prediction, we consider different amounts of structural uncertainty such that it will result in an unbiased estimation.

As a demonstration example, we present results for an exploratory (small) ensemble calculation. Details of the perturbations for the eight different samples considered are listed in Tab. 1. For each sample, uniform independent random values are obtained for discrepancy in tensor magnitude ($\Delta\tau_{kk}^{sgs}$), relative distance (Δ_B) and target vertex ($\mathbf{x}^t$) of anisotropy uncertainty, and permutation (Perm.) in tensor orientation. The intervals of the perturbation parameters are based on the limiting values of the sensitivity analysis discussed in Sec. 5.1.

The ensemble effects of the combined perturbations are shown in Fig. 9 for the averaged streamwise velocity profile (a) and rms velocity fluctuations (b, c, d). The first observation is that there is very good agreement between the mean and DNS velocity profiles in the viscous and buffer layers, as well as in the log-law region up to $y^+ \approx 100$. In addition, the profiles of minimum and maximum prediction completely envelope the DNS solution. This is not the typical result obtained from ensemble calculations based on sets of LES models that do not consider variations in all the degrees of freedom. The second important observation is that velocity fluctuations present different variability behavior with respect to individual perturbations. For instance, overprediction of streamwise fluctuation peak ($y^+ \approx 15$) is significantly reduced. Moreover, the minimum and maximum predictions are able to envelope the DNS result for practically all y^+. Different variability is observed also for the vertical and spanwise fluctuations. In particular, the prediction envelope in the vertical direction considers solutions with larger fluctuations than the predictions for individual perturbations along the y-axis, especially close to the wall ($y^+ \approx 50$). A similar trend is obtained for the spanwise fluctuations, however, not for the near-wall region. This result is commonly observed in LES of turbulent channel flow and, as discussed in the Appendix and shown in Fig. 10, is mainly related to the incapacity of the meshes typically considered to properly capture the large scales in the spanwise direction, viz. this inaccuracy depends on the resolved scales and not on the SGS modeling.

6. Conclusions and future work

The aim of this work has been to develop a framework for estimating structural uncertainty in LES closures that goes beyond traditional non-intrusive sensitivity studies. The approach proposed is based on decomposing the SGS stress tensor such that incertitude can be independently injected as discrepancy in magnitude (trace), anisotropy (eigenvalues), and orientation (eigenvectors) of the normalized turbulent stresses with respect to a particular tensor state. In addition, physically reasonable bounds for estimating uncertainty are proposed for the six degrees of freedom of the methodology.

The performance of the UQ framework has been tested by computing LES of wall-resolved turbulent channel flow, and comparing the solution of the perturbed cases to the results predicted by the base SGS model (WALE) and DNS reference data. The numerical results focus on spatially uniform perturbations to the magnitude, shape, and orientation of the SGS stress tensor. Three main outcomes have been observed in the case of well-resolved calculations. First, the effects of perturbing the base-model in terms of magnitude discrepancy are small, especially in comparison to perturbations to the shape and orientation. Second, anisotropy perturbations to the one-component vertex result in flow laminarization, while perturbations to the three-component vertex increase the levels of turbulence, however, in a much lesser degree. Third, orientation incertitude by means of permutation three results in sustained introduction of kinetic energy from the modeled to the resolved scales (backscatter) that energizes the flow, whereas

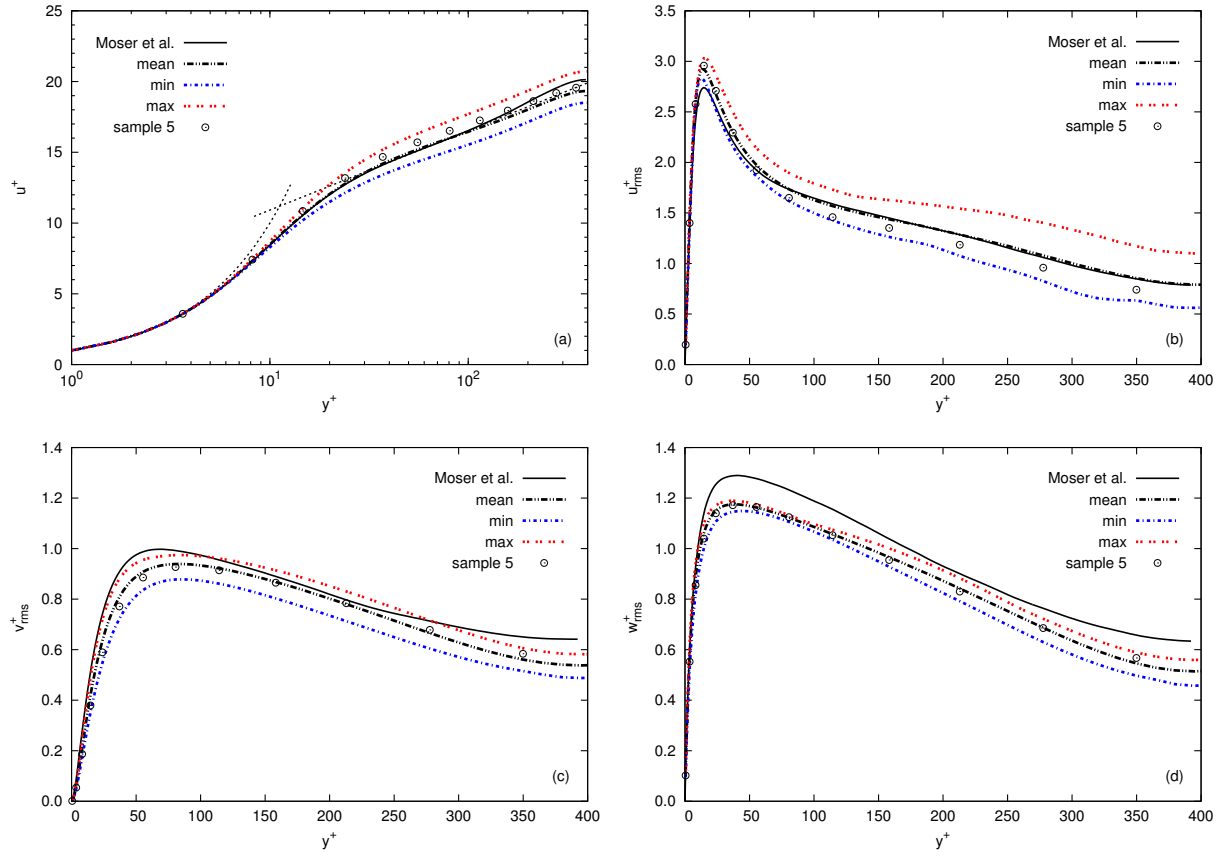

Figure 9: Mean and envelope solutions of the ensemble perturbation calculation (quantities in wall units). (a) Averaged streamwise velocity profile. (b) Streamwise rms velocity fluctuation. (c) Vertical rms velocity fluctuation. (d) Spanwise rms velocity fluctuation. DNS data from [48] (solid line), mean solution and minimum and maximum bounds (dashed lines), sample 5 result (circles).

permutation one is equivalent to eddy-viscosity-type models and acts as an energy sink (forward-scatter). Moreover, the ensemble calculation exposes the importance of considering combinations of perturbations as different variability is observed for first- and second-order statistics. From a general perspective, the overall numerical study demonstrates the capability of the strategy to provide bounds for the QoI (averaged streamwise velocity) that envelop the base-model prediction and DNS solution. This feature is of great importance for utilizing the proposed UQ estimation approach in computational studies involving engineering applications. Furthermore, the advantage of decomposing the tensor in magnitude, shape and orientation is illustrated by giving direct physical interpretation of the effects of the perturbations introduced.

Ongoing work is focused on analyzing the performance of the methodology for complex flow configurations, as well as formal strategies for combining different types of perturbations. In addition, parallel studies are also being performed to incorporate the numerical uncertainty resulting from the discretization approximations into the current structural framework. Future work will concentrate on developing transport equations for the parameters of the methodology such that injection of incertitude is restricted to regions of the flow where the models are expected to provide less accurate predictions. For example, regions of transverse (Prandtl's second kind of secondary flow) mean motion in turbulent square duct flow, thin separating shear layers in flows over circular cylinders, or reverse vorticity zones in flows over backward-facing steps.

Acknowledgments

This investigation was funded by the United States Department of Energy's (DoE) National Nuclear Security Administration (NNSA) under the Predictive Science Academic Alliance Program II (PSAAP II) at Stanford University.

Appendix. Mesh convergence study

The main objective of this work is to introduce a framework to analyze sensitivity to structural uncertainty in LES closures. Of particular interest is the case of reasonably well-resolved LES calculations in which a balance between overall accuracy and computational cost is a critical aspect. In this regard, a mesh convergence study is presented here for the computational case considered in the numerical experiments section.

The problem under consideration is LES of channel flow at $Re_\tau = 395$. Details of the computational setup are described in Sec. 5. Differences between three increasingly finer meshes are discussed and compared against DNS data from Moser et al. [48]. The size of the meshes in the streamwise, vertical and spanwise directions are $64\times64\times64$, $64\times128\times64$, and $64\times128\times96$. The meshes are uniform in the streamwise and spanwise directions, while stretched following a hyperbolic tangent distribution in the wall-normal direction. The latter mesh is chosen for the numerical tests of structural uncertainty.

Results of averaged streamwise velocity profile (a) and rms velocity fluctuations (b, c, d) for the three meshes considered are shown in Fig. 10. The first observation is that the magnitudes and trends of the results are in accordance with equivalent LES calculations reported in the literature; for example in Gullbrand & Chow [50]. The (1) averaged streamwise velocity profile tends to be overpredicted starting from $y^+ \approx 10$, (2) there is an overprediction in streamwise velocity fluctuation at $y^+ \approx 15$, and (3) the vertical and spanwise fluctuations are underpredicted for all y^+. However, a clear difference in trend is observed between averaged velocity profile and fluctuations. Irrespective of the spatial direction, refining the mesh improves the LES prediction of averaged velocity. Conversely, refining the mesh in the vertical direction by a factor of two does not improve significantly the accuracy in velocity fluctuation prediction, especially in the near-wall region ($y^+ \approx 50$), while a notable improvement is achieved when refining the mesh in the spanwise direction. An interpretation of this behavior in channel flow is that turbulence tends to organize in long streaks along the streamwise direction. Consequently, a relatively small number of gridpoints is sufficient to capture the evolution of the large structures in the streamwise direction. By contrast, the turbulent eddies in the spanwise direction are small, and therefore many more gridpoints are required per spatial length to properly capture them. Typical meshes considered in LES calculations are not fine enough in the spanwise direction, and consequently large scales tend to survive longer due to the incapacity of the grids to break them. In other words, the overprediction in streamwise and underprediction in vertical and spanwise velocity fluctuations is mainly related to the ratio between mesh resolution and large scales in the spanwise direction, and is effectively independent from the subgrid-scale modeling.

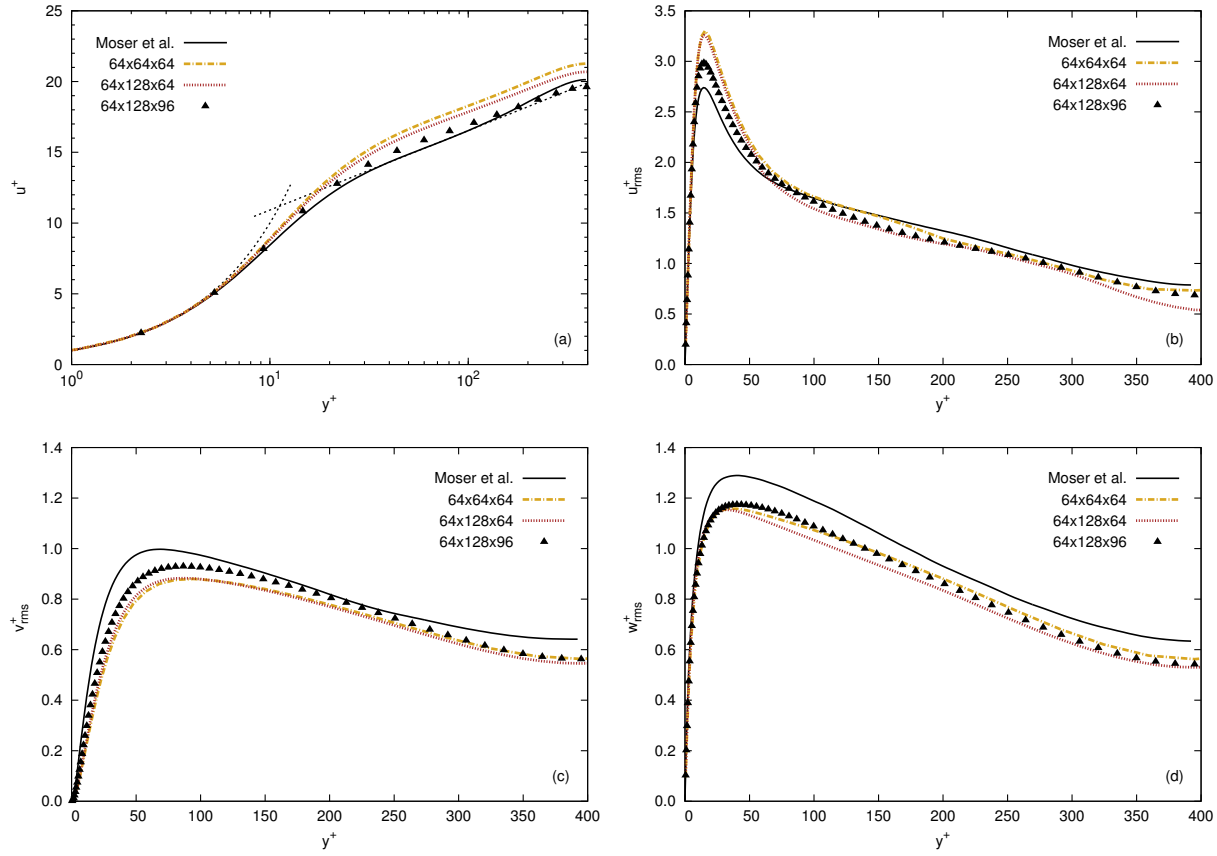

Figure 10: Mesh convergence study for LES of channel flow at $Re_\tau = 395$ (quantities in wall units). (a) Averaged streamwise velocity profile. (b) Streamwise rms velocity fluctuation. (c) Vertical rms velocity fluctuation. (d) Spanwise rms velocity fluctuation. DNS data from [48] (solid line), base-model mesh (solid triangles), coarser meshes (dashed lines).

References

[1] S. Hermeth, G. Staffelbach, L. Y. M. Gicquel, T. Poinsot, LES evaluation of the effects of equivalence ratio fluctuations on the dynamic flame response in a real gas turbine combustion chamber, P. Combust. Inst. 34 (2013) 3165–3173.

[2] G. Bulat, E. Fedina, C. Fureby, U. Stopper, Reacting flow in an industrial gas turbine combustor: LES and experimental analysis, P. Combust. Inst. 35 (2015) 3175–3183.

[3] M. Masquelet, J. Yan, A. Dord, G. Laskowski, L. Shunn, L. Jofre, G. Iaccarino, Uncertainty quantification in large eddy simulations of a rich-dome aviation gas turbine, in: Proc. ASME Turbo Expo 2017, GT2017-64835, pp. 1–11.

[4] Workshop on extreme-scale solvers: transition to future architectures, Technical Report, U.S. Department of Energy, Office of Advanced Scientific Computing Research, 2012.

[5] S. Ghosal, An analysis of numerical errors in large-eddy simulations of turbulence, J. Comput. Phys. 125 (1996) 187–206.

[6] J. Meyers, B. J. Geurts, M. Baelmans, Database analysis of errors in large-eddy simulation, Phys. Fluids 15 (2003) 2740.

[7] M. Meldi, D. Lucor, P. Sagaut, Is the Smagorinsky coefficient sensitive to uncertainty in the form of the energy spectrum?, Phys. Fluids 23 (2011) 125109.

[8] J. Meyers, P. Sagaut, Evaluation of Smagorinsky variants in large-eddy simulations of wall-resolved plane channel flows, Phys. Fluids 19 (2007) 095105.

[9] J. Meyers, P. Sagaut, Is plane-channel flow a friendly case for the testing of large-eddy simulation subgrid-scale models?, Phys. Fluids 19 (2007) 048105.

[10] M. C. Dunn, B. Shotorban, A. Frendi, Uncertainty quantification of turbulence model coefficients via latin hypercube sampling method, J. Fluids Eng. 133 (2011) 041402.

[11] D. Lucor, J. Meyers, P. Sagaut, Sensitivity analysis of large-eddy simulations to subgrid-scale-model parametric uncertainty using polynomial chaos, J. Fluid Mech. 585 (2007) 255–280.

[12] S. Cheung, T. Oliver, E. Prudencion, S. Pridhomme, R. Moser, Bayesian uncertainty analysis with applications to turbulence modeling, Reliab. Eng. Syst. Saf. 96 (2011) 1137–1149.

[13] S. Völker, R. Moser, P. Venugopal, Optimal large eddy simulation of turbulent channel flow based on direct numerical simulation statistical data, Phys. Fluids 14 (2002) 3675–3691.

[14] N. A. Phillips, Models for weather prediction, Annu. Rev. Fluid Mech. 2 (1970) 251–292.

[15] C. E. Leith, Objective methods for weather prediction, Annu. Rev. Fluid Mech. 10 (1978) 107–128.

[16] C. Gorlé, G. Iaccarino, A framework for epistemic uncertainty quantification of turbulent scalar flux models for Reynolds-averaged Navier-Stokes simulations, Phys. Fluids 25 (2013) 055105.

[17] M. Emory, J. Larsson, G. Iaccarino, Modeling of structural uncertainties in Reynolds-averaged Navier-Stokes closures, Phys. Fluids 25 (2013) 110822.

[18] O. V. Vasilyev, T. S. Lund, P. Moin, A general class of commutative filters for LES in complex geometries, J. Comput. Phys. 146 (1998) 82–104.

[19] A. L. Marsden, O. V. Vasilyev, P. Moin, Construction of commutative filters for LES on unstructured meshes, J. Comput. Phys. 175 (2002) 584–603.

[20] A. Leonard, Energy cascade in large-eddy simulations of turbulent fluid flows, Adv. Geophys. A 18 (1974) 237–248.

[21] T. S. Lund, The use of explicit filters in large eddy simulation, Comput. Math. Appl. 46 (2003) 603–616.

[22] R. S. Rogallo, P. Moin, Numerical simulation of turbulent flow, Annu. Rev. Fluid Mech. 16 (1984) 2150.

[23] R. A. Clark, J. H. Ferziger, W. C. Reynolds, Evaluation of subgrid-scale models using an accurately simulated turbulent flow, J. Fluid Mech. 91 (1979) 1–16.

[24] J. Bardina, J. H. Ferziger, W. C. Reynolds, Improved subgrid scale models for large eddy simulation, in: Proc. AIAA 13th Fluid & Plasma Dynamics Conference, pp. 1–10.

[25] Y. Zang, R. L. Street, J. R. Koseff, A dynamic mixed subgrid-scale model and its application to turbulent recirculating flows, Phys. Fluids A 5 (1993) 3186–3195.

[26] C. Meneveau, J. Katz, Scale-invariance and turbulence models for large-eddy simulation, Annu. Rev. Fluid Mech. 32 (2000) 1–32.

[27] J. Smagorinsky, General circulation experiments with the primitive equations. I. The basic experiment, Mon. Weather Rev. 91 (1963) 99–164.

[28] M. Germano, U. Piomelli, P. Moin, W. Cabot, A dynamic subgrid-scale eddy viscosity model, Phys. Fluids A 3 (1991) 1760–1765.

[29] F. Nicoud, F. Ducros, Subgrid-scale stress modelling based on the square of the velocity gradient, Flow Turbul. Combust. 62 (1999) 183–200.

[30] F. Nicoud, H. B. Toda, O. Cabrit, S. Bose, J. Lee, Using singular values to build a subgrid-scale model for large eddy simulations, Phys. Fluids 23 (2011) 085106.

[31] W. Rozema, H. J. Bae, P. Moin, R. Verstappen, Minimum-dissipation models for large-eddy simulation, Phys. Fluids 27 (2015) 085107.

[32] L. Jofre, O. Lehmkuhl, J. Ventosa, F. X. Trias, A. Oliva, Conservation properties of unstructured finite-volume mesh schemes for the Navier-Stokes equations, Numer. Heat Transfer, Part B 65 (2014) 53–79.

[33] A. Yoshizawa, Statistical theory for compressible turbulent shear flows, with the application to subgrid modeling, Phys. Fluids 29 (1986) 2152–2164.

[34] P. Moin, K. Squires, W. Cabot, S. Lee, A dynamic subgrid-scale model for compressible turbulence and scalar transport, Phys. Fluids A 3 (1991) 2746–2757.

[35] U. Schumann, Realizability of Reynolds-stress turbulence models, Phys. Fluids 20 (1977) 721–725.

[36] B. Vreman, B. Geurts, H. Kuerten, Realizability conditions for the turbulent stress tensor in large-eddy simulation, J. Fluid Mech. 278 (1994) 351–362.

[37] J. L. Lumley, G. Newman, The return to isotropy of homogeneous turbulence, J. Fluid Mech. 82 (1977) 161–178.

[38] K.-S. Choi, J. L. Lumley, The return to isotropy of homogeneous turbulence, J. Fluid Mech. 436 (2001) 59–84.

[39] S. Banerjee, R. Krahl, F. Durst, C. Zenger, Presentation of anisotropy properties of turbulence, invariants versus eigenvalues approaches, J. Turbul. 8 (2007) 1–27.

[40] G. Kindlmann, Superquadric tensor glyphs, in: Proc. 6th Joint Eurographics-IEEE TCVG Conference, pp. 147–154.
[41] T. Project, Teem: Tools to process and visualize scientific data and images, 2003.
[42] S. Stolz, A. Adams, An approximate deconvolution procedure for large-eddy simulation, Phys. Fluids 11 (1999) 1699–1701.
[43] S. B. Pope, Turbulent flows, Cambridge University Press, 2000.
[44] U. Piomelli, W. Cabot, P. Moin, S. Lee, Subgrid-scale backscatter in turbulent and transitional flows, Phys. Fluids 3 (1991) 1766–1771.
[45] J. B. Lasserre, A trace inequality for matrix product, IEEE Trans. Autom. Control 40 (1995) 1500–1501.
[46] T. S. Lund, S. Ghosal, P. Moin, Numerical experiments with highly variable eddy viscosity model, Eng. Appl. LES 162 (1993) 7–11.
[47] S. P. Domino, Sierra Low Mach Module: Nalu Theory Manual 1.0, Technical Report SAND2015-3107W, Sandia National Laboratories, Unclassified Unlimited Release (UUR), 2015.
[48] R. D. Moser, J. Kim, N. N. Mansour, Direct numerical simulation of turbulent channel flow up to $Re_\tau = 590$, Phys. Fluids 11 (1999) 943–945.
[49] D. Chapman, G. Kuhn, The limiting behavior of turbulence near a wall, J. Fluid Mech. 170 (1986) 265–292.
[50] J. Gullbrand, F. K. Chow, The effect of numerical errors and turbulence models in large-eddy simulations of channel flow, with and without explicit filtering, J. Fluid Mech. 495 (2003) 323–341.